Site-specific Raman spectroscopy and chemical dynamics of nanoscale interstitial systems

2005 J. Phys.: Condens. Matter 17 R333

(http://iopscience.iop.org/0953-8984/17/7/R02)

INSTITUTE OF PHYSICS PUBLISHING JOURNAL OF PHYSICS: CONDENSED MATTER

J. Phys.: Condens. Matter **17** (2005) R333–R355 doi:10.1088/0953-8984/17/7/R02

TOPICAL REVIEW

Site-specific Raman spectroscopy and chemical dynamics of nanoscale interstitial systems

H Peter Lu

Pacific Northwest National Laboratory, Fundamental Science Division, Richland, WA 99352, USA

E-mail: peter.lu@pnl.gov

Received 19 August 2004, in final form 19 January 2005
Published 4 February 2005
Online at stacks.iop.org/JPhysCM/17/R333

Abstract

Site-specific spectroscopy is critical for a molecular-level understanding of the mechanisms and dynamics of the inhomogeneous chemical processes crucial for catalysis, surface and interfacial chemistry, and membrane protein dynamics in living cells. Surface-enhanced Raman scattering (SERS) spectroscopy and microscopy combined with atomic force microscopy (AFM) using metal-coated AFM tips have proven to be powerful in spectroscopic analysis of inhomogeneous processes, providing correlated topographic and spectroscopic information at the nanoscale from sites in highly heterogeneous environments. It has recently been observed that SERS spectral fluctuations are pertinent to site-specific spectroscopy and microscopy. Such fluctuations are important in that they hold promise for the study of molecular structure and dynamics at a single-molecule level. This article reviews our recent work on characterization and analysis of SERS spectral fluctuation dynamics at the nanoscale in metallic interstitial sites. Fluctuations were found to accompany nanoscale confined electromagnetic near-field enhancement. The result of such confinement is that only a few molecules dominate the far-field SERS spectral signal detected in microscopic measurements that probe one nanoscale 'hot' site at a time. The fluctuation amplitude significantly decreased with the number of molecules confined at the nanoscale-local field. A new AFM-coupled two-channel photon time-stamping system, enabling *in situ* correlation of the topographic and spectroscopic information for single nanoparticle clusters, was used to record the Raman intensity fluctuation trajectories at a sub-microsecond resolution. Experimentally, we found that SERS fluctuation dynamics are highly inhomogeneous amongst nanocluster interstitial sites although molecular translational and rotational motions at the interstitial sites can account for the SERS spectral fluctuations. To further understand these fluctuations at the nanoscale interstitial sites and nanostructures, field enhancement and field distribution at different interstitial site topographies and

rough fractal surfaces were studied using finite element method computational simulation in a classic electrodynamics approach.

(Some figures in this article are in colour only in the electronic version)

Contents

1. Introduction

Nanoscale observations of chemical and physical processes at interfaces and surfaces typically encounter significant spatial inhomogeneities, such as defects, lattices, kinks, etc, that can dominate chemical activities even though such sites may have only low distribution densities on surfaces or at interfaces. Characterizing the chemistry at these specific sites promises to provide a mechanistic and detailed understanding of catalysis and interfacial chemical reactions. Our knowledge of chemically active sites has been tremendously advanced from the extensive studies that characterize topographic features at high spatial resolutions using atomic force microscopy (AFM) and scanning tunnelling microscopy (STM) and that have correlated chemical and biological information with topographic imaging [1]. Types of optical spectroscopy, such as fluorescence and Raman near-field scanning optical microscopy [2–5], AFM–metallic tip surface-enhanced Raman spectroscopy (AFM–SERS) [6–16], and AFM–metallic tip enhanced fluorescence lifetime imaging microscopy (AFM–FLIM) [17–20], have proven to be powerful means of chemical and biological characterization. However, the primary challenge for such site-specific characterization remains correlating topographic and spectroscopic characterizations at the same sites. There has been extensive Raman spectral analysis of surface chemical activities at specific sites and at the nanometre scale [21–35]. Another important field of site-specific spectroscopy is its application to single-molecule studies of enzymatic reactions and protein conformational dynamics involving protein–protein interactions, protein–DNA interactions, and membrane protein dynamics [36–45].

Raman has been a powerful approach in analysing chemical states and the processes of molecules on surfaces and at interfaces [21–35]. Because Raman spectra contain detailed information on molecular structure and energetic states [46–48], such as the protein conformation changes, protein structure changes, molecular interactions, and chemical reaction processes, they are useful in investigating specific sites at the nanoscale. Mode-specific characterization of interfacial electron transfer is a significant example [27, 34, 35]. Although Raman scattering typically has 10^{14} times smaller cross-sections than fluorescence, metallic surface enhancement, or resonance enhancement, the Raman cross-section can be as large as

the fluorescence cross-section in some cases, such as with reported single-molecule Raman scattering detections [49–63].

The SERS signal is presumably proportional to the fourth power of the excitation field [21–23], and the field distribution is typically inhomogeneous at the nanoscale as the SERS enhancing substrates are typically rough noble metallic surfaces or nanoparticles. The inhomogeneous enhancement amongst the specific sites is due to several possible factors, including their different structures [60–66], surface plasmon frequencies [21–26, 53–57], surface electron work functions [24, 51], electronic coupling [27–33] between the adsorbed molecules and the local surface environment. In recent years, SERS spectral fluctuation has been observed during microscopic imaging of the individual 'hot' spots at the diffraction-limited laser focus. Under such experimental conditions, the SERS 'hot' spots were typically nanoscale interstitial sites in nanoparticle clusters or nanostructures. The SERS spectral fluctuations involve Raman frequency fluctuation, intensity fluctuation, and peak-to-peak intensity ratio fluctuation [49–63].

There is still no direct way to correlate the configuration and field enhancement, especially when the active sites are typically at the nanoscale. Apparently, various nanoscale roughnesses of the surfaces either at interstitial sites or at the sites on fractal surfaces play significant roles in the field enhancement. However, in experiments the roughness is hard to quantify and to correlate with field distributions. While the Mie theory can assess enhancements for regular configurations and topographies of specific sites, it is not as effective when applied to complex configurations and structures. On the other hand, a few computational simulations have provided detailed characterizations of enhancements or near-field electromagnetic field distributions [61, 63, 67–72].

The following sections review our recent work on site-specific spectroscopy, first presenting the microscopic spectroscopy technique that enables us to conduct site-specific Raman spectroscopy and then focusing on SERS spectral fluctuation phenomena and site-specific SERS fluctuation dynamics. Finally, the studies are reviewed that have characterized local electromagnetic field enhancement associated with various site configurations and the topographies of metallic nanoparticles and nanostructures. The perspective of the broad applications of the knowledge obtained and technology developed in this research area are also discussed.

2. Atomic force microscopy correlated multi-optical channel spectroscopy

2.1. Experimental measurements

Recent developments in optics, microscopy, spectroscopy, and electronics have provided unprecedented capabilities in topographic and spectroscopic characterization of catalytic surfaces and catalysis reactions at nanometre scales, wide dynamic time ranges, and single-molecule sensitivity. Raman spectroscopy and microscopic imaging have the advantage of site-specific chemical identification, with sensitivity that has reached the single-molecule level, as demonstrated for several chemical species [49–60]. Significant progress has been made on coupling near-field enhancement to Raman spectroscopy and imaging in order to demonstrate high spatial resolution beyond the optical diffraction limit and even to reach typical AFM spatial resolution [1–20]. A few articles have presented broad reviews of recent work [1–5]. Here, we focus our discussion on our recent work in this area.

One of the most promising approaches is metallic tip-enhanced Raman microscopy using nanoscale-curvatured Ag or Au metallic-coated AFM tips [1–20, 60–63], coupled with an inverted optical microscope that has high numerical aperture objectives capable of

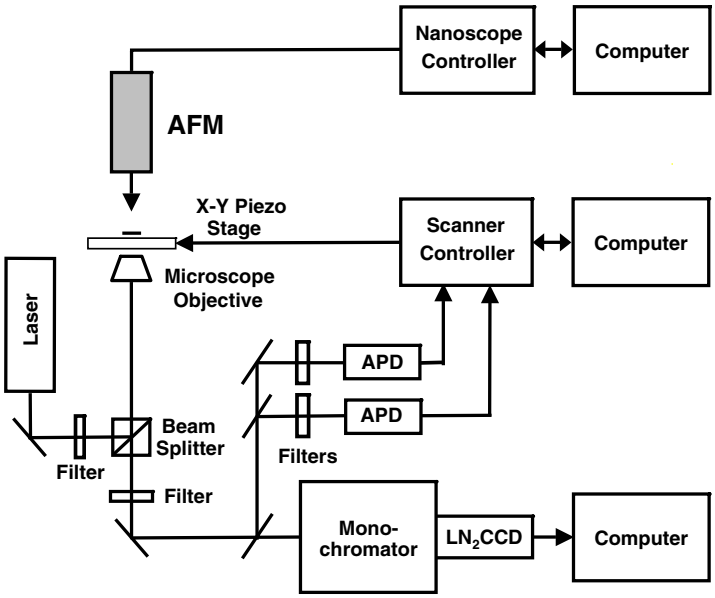

Figure 1. Schematic diagram of an AFM–SERS imaging and site-specific spectroscopy experimental set-up. Multiple optical detection channels are correlated with an AFM topographic imaging channel. Raman 2D imaging and spectroscopy are obtained by using a CCD camera coupled with a monochromator. Time-correlated single-photon counting and photon-stamping detection using a two-channel APD detection module can record each photon arrival time. We used narrow band filters to selectively detect a specific Raman band and its adjacent background, with the Raman signal picked up by real-time or off-line subtraction of the Raman band signals from the background signal.

ultrasensitive single-molecule imaging and spectroscopy at nanoscale topographical specificity. The site-specific spectroscopic imaging was achieved by a combination of two microscopes, an atomic force microscope and an inverted far-field optical microscope with single-molecule spectroscopic sensitivity, in an over–under arrangement, set to imaging the same point in space. The AFM (Bioscope, Digital Instruments Inc., Veeco Metrology Group), using a Nanoscope IIIa controller, was mounted on a homemade micro-mechanical stage. The scanning confocal Raman microscope was based on an inverted optical microscope (Axiovert 135, Zeiss) and a piezoelectric x–y sample scanner (Physik Instrument, Polytech), driven by an independent homemade scanning controller and software (figure 1) [17, 19, 20, 60, 62]. In addition to its single-molecule spectroscopic capabilities, which included a two-channel photon time-stamping detection system [17, 40–42, 60, 62], this set-up allowed temporal and spatial characterizations of surface-enhanced Raman scattering at interstitial sites and surface nanoscale structures.

Spectral intensity time trajectories could be simultaneously recorded for the Raman channel and the emission background channel. The off-line subtraction of the two trajectories gave a pure Raman trajectory with sub-microsecond time resolution (figure 1). The output from these two photodiodes was directed toward a data-collection system that enabled synchronized dual-channel single-photon event detection. The Raman spectra were collected using a liquid-N_2-cooled CCD (LN/CCD-1340/400-EB/1, Roper Scientific) mounted on the exit port of the monochromator. We have also used a holographic imaging spectrograph (Kaiser Holospec f/1.8i VIS, Kaiser Optical Systems, Inc.), which has a higher transmission throughput to detect a weaker Raman spectral signal.

The tapping-mode or torsional-resonance-mode (TRmode) AFM module on top of the optical microscope stage (figure 1) has been used to correlate the two-dimensional Raman image with the AFM topographical image. In this way, the nanoscale topographic and Raman spectroscopic characterization have been correlated *in situ* for the same measurement area with an overlap precision of 10 nm or better (figure 1), providing detailed information on surface nanostructure-dependent Raman spectral fluctuation dynamics [60, 62]. This set-up enabled us to obtain Raman spectra, Raman 2D images, Raman band temporal trajectories, and nanoparticle topographic images of single isolated nanoparticle clusters adsorbed with organic and biological molecules.

2.2. Model analysis of Raman scattering at interstitial sites of nanoparticle pairs

The SERS scattering intensity and field distribution under laser excitation at a nanoscale interstitial site can be calculated based on Mie scattering theory [60, 62, 73–76] to solve the scattering equation for the electric field. To apply Mie theory to SERS scattering for metallic nanoparticles or nanostructures, some system complexities are typically excluded from the model, e.g., the non-uniform refractive index gradient, non-spherical geometry, multiple-sphere clusters, irregular nanoscale structure shapes, and diffraction-limited Gaussian laser intensity distribution. Besides the 'classic' electromagnetic field enhancement, there are also chemical enhancement effects that are significant and inhomogeneous at the nanoscale, such as the surface work function and the electronic coupling between the chemically adsorbed molecules and the nanoparticle plasmon. These complexities can significantly change the local electromagnetic field enhancement profile. Nevertheless, the scattering cross-section and intensity within the integrated solid angle of collection, calculated from a simplified Mie multiple-scattering theory, are essentially correct [60, 62, 73–76] and valuable for an investigation into spectral fluctuation dynamics due to molecule motions in a local field [60, 62]. The integral equation describing the scattered optical field, $\mathbf{E}^{\text{out}}$, as a function of the incident optical field, $\mathbf{E}^{\text{in}}$, is

$$\mathbf{E}^{\text{out}}(\mathbf{r},\omega) = \mathbf{E}^{\text{in}}(\mathbf{r},\omega) + k^2 \int \mathrm{d}\mathbf{r}'\, G(\mathbf{r},\mathbf{r}')[1 - \varepsilon(\omega,\mathbf{r}') - 4\pi\chi(\omega,\mathbf{r}')] \cdot \mathbf{E}^{\text{out}}(\mathbf{r}',\omega) \tag{1}$$

where $G(\mathbf{r},\mathbf{r}')$ is the Green's function propagating the wavefield

$$G(\mathbf{r},\mathbf{r}') = -\frac{\mathrm{e}^{\mathrm{i}k|\mathbf{r}-\mathbf{r}'|}}{4\pi|\mathbf{r}-\mathbf{r}'|} \tag{2}$$

where $\varepsilon(\omega,\mathbf{r})$ is the dielectric response of the metallic spheres, $\chi(\omega,\mathbf{r})$ is the polarization tensor for the molecular response, $\mathbf{k}$ is the magnitude of the wavevector, and ω is the frequency. The integral equation is solved by placing a vector harmonic basis on each of the sphere positions $\mathbf{R}_\mu$. In our study, we considered the incident field $\mathbf{E}^{\text{in}}(\mathbf{r}) = \mathbf{E}_0\mathrm{e}^{\mathrm{i}\mathbf{k}\cdot\mathbf{r}}$. We used the experimental wavelength of incident light, $\lambda = 514.5$ nm, where Ag has a dielectric response $\sqrt{\varepsilon} = 0.05 + 3.266\mathrm{i}$. We took $\mathbf{k} = (0,0,k)$ and $\mathbf{E}_0 = (E_0,0,0)$, with a single molecule located at the origin. The molecular polarizability tensor in the molecular frame was taken to be

$$a_{\text{m}} = \alpha_{\text{m}} \begin{pmatrix} 1 & 0 & 0 \\ 0 & 1 & 0 \\ 0 & 0 & 0 \end{pmatrix}$$

which corresponds to a molecule with isotropic polarization in the x–y plane. Two Ag spheres are positioned at $\mathbf{R}_{\text{s}} = (R_{\text{s}} + d/2, 0, 0)$ and $\mathbf{R}_{\text{s}} = (R_{\text{s}} - d/2, 0, 0)$, where R_{s} is the radius of each sphere and d is the distance between the spheres. We considered the case of $R_{\text{s}} = 40$ nm

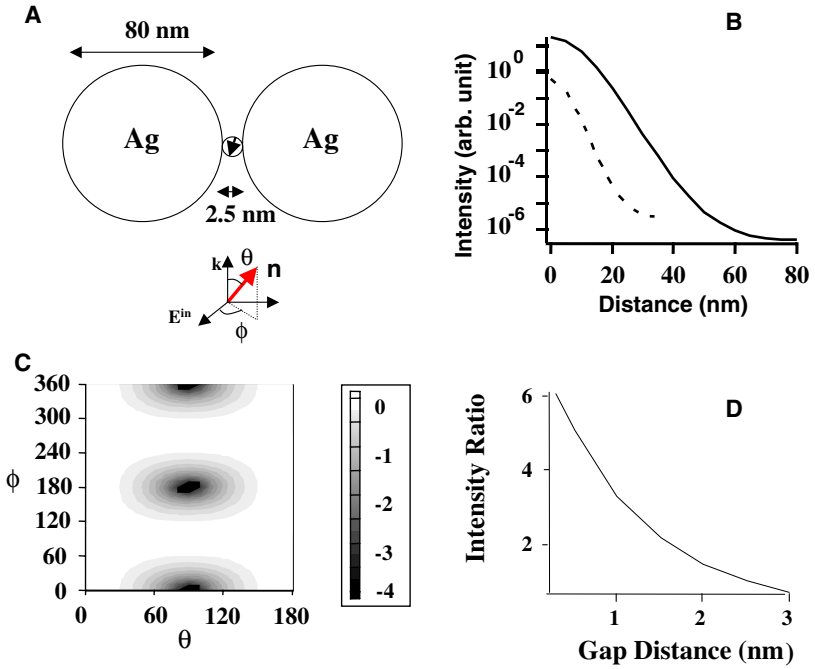

Figure 2. (A) Schematic diagram for the interstitial site (2.5 nm gap) of a cluster of two 80 nm diameter Ag spheres. In our simulations, the polarization axis of the excitation electric field, E, is parallel with the minimum particle separation distance vectors. (B) Simulated spatial distance dependence of SERS intensity of a dipole at the interstitial site of two Ag spheres of 80 nm (solid curve) and 40 nm (dashed curve) diameters at 514.5 nm excitation. (C) Simulated molecular orientation-angle θ- and ϕ-dependent SERS intensity of a dipole at the interstitial site. The excitation wavelength is 514.5 nm. The intensity bar is at log scale from 1 to 10^{-4}. (D) Simulated interstitial gap-distance dependence of the SERS intensity for two 40 nm Ag spheres. The intensity ratio is the ratio of the intensity at different gap distances versus the intensity at the gap distance of 2.5 nm and $\phi = \theta = 0$. (Adapted with permission from the American Chemical Society from [60] and [62].)

(and $R_s = 20$ nm) and $d = 2.5$ nm (figure 2(A)). The Raman signal intensity was determined from

$$I = \int_0^{2\pi} \mathrm{d}\phi \int_{2\pi/3}^{\pi} \sin(\theta)\, \mathrm{d}\theta\, \hat{\mathbf{r}} \cdot \mathbf{S}$$

where $\mathbf{S}$ is the Poynting vector of the scattered field. The intensity versus position of the molecule, $\mathbf{R}$, and the orientation of the molecule described in terms of the Euler angles, $(\theta_\mu, \phi_\mu, \psi_\mu)$, and the position of the metallic spheres, $\mathbf{R}_\mu$, were calculated. Figure 2(B) shows that the Raman scattering intensity changes about 10^6-fold as the scattering site departs from the centre of the interstitial site. It is evident that the Raman scattering signal is dominated by the molecules at the nanoscale interstitial sites. On the other hand, we showed a less dramatic change of the Raman scattering intensity as the interstitial gap changed (figure 2(C)); this result was obtained by considering only the electromagnetic field enhancement. The gap-size dependence could be much stronger if chemical enhancement were also considered [21–23]. Figure 2(D) shows that the Raman scattering intensity is highly sensitive to the orientation of a molecule transition dipole at an interstitial site, and an intensity change of four orders of

magnitude can be produced by molecular rotational motions. The orientation dependence of the Raman scattering intensity is essentially the same for different sizes of nanoparticles if we consider the molecule to be a point dipole illuminated under a plane electromagnetic wave.

3. Surface-enhanced Raman scattering spectral fluctuation at nanoscale sites

SERS is typically measured at Ag or Au metallic surfaces and enhanced by near-field electromagnetic field and chemical interactions between the molecules and the substrate [21–26]. SERS microscopy has been developed and applied extensively at optical-diffraction-limited spatial resolution [6–16, 20, 60, 62]. Interestingly, SERS spectral fluctuation has often been observed at a spatially confined 'hot spot' of nanoscale interstitial sites at metallic nanoparticle clusters [49–63]. The SERS spectral fluctuations involve Raman shift, peak intensity, peak-to-peak intensity ratio, and peak bandwidth [49–63]. Although a SERS fluctuation is typically observed under a microscope, this phenomenon should be intrinsic to the SERS in general. However, it can only be significant when both the number of the Raman active molecules and the sampling area are small. Generally, Raman spectral fluctuations can be expected when the number of Raman active molecules is sufficiently low; fluctuations are averaged out when the number of Raman active molecules is high. It is important to understand these fluctuations because they contain rich information about Franck–Condon coupling and nuclear displacement in a chemical and biological molecular process at the specific sites [27–31, 35].

It has been shown that SERS fluctuations comprise both photoinduced and spontaneous contributions [51, 56, 59, 60, 62]. The origin of SERS fluctuations can be accounted for either by the surface charge transfer between the adsorbed molecule and the metallic surface [51, 56], the inhomogeneous surface function of the substrates [60, 62], or the rotational and translational motions of adsorbed molecules [50, 51, 56, 59, 60, 62]. We have reported studies of SERS intensity fluctuations for both single and multiple molecules of R6G and cytochrome c at Ag nanoclusters. Our experiments suggested that

(1) the fluctuation is inhomogeneous and nanostructure dependent;
(2) the fluctuation originates from the nanoscale high field enhancement at the interstitial sites and that the nanoscale confinement of the site limits the number of the adsorbed molecules exposed to the high electric field; and
(3) the fluctuation is not necessarily associated only with single-molecule SERS and that SERS fluctuations can be observed with even half-monolayer coverage of the Raman active molecules on the nanoparticle clusters because the nanoscale interstitial sites actually confirm that the SERS enhanced signal is predominantly from a few molecules.

These findings provide insight into the SERS fluctuation dynamics and mechanism and offer help in studying low-concentration molecules in a heterogeneous environment, at catalytic reaction surfaces [16] and on biological membranes, with vibrational spectroscopy and imaging [84].

To investigate a single interstitial junction at the bi-cluster of silver nanoparticles, we [60, 62], as well as other laboratories [51, 52, 56, 59], have found that the SERS hot spots are typically nanoclusters. Our AFM-coupled Raman microscope enabled us to identify the topographic structure of these hot spots. Figures 3(A)–(D) represent a typical AFM–SERS correlated image of the Ag nanoparticle clusters, showing that there are about ten nanoclusters and a number of single nanoparticles in the imaging area of the sample. However, only one cluster shows a strong Raman signal (figures 3(A) and (B)). AFM close-up imaging identified that hot spot as a bi-nanoparticle cluster with a gap of less than 2 nm at the interstitial site

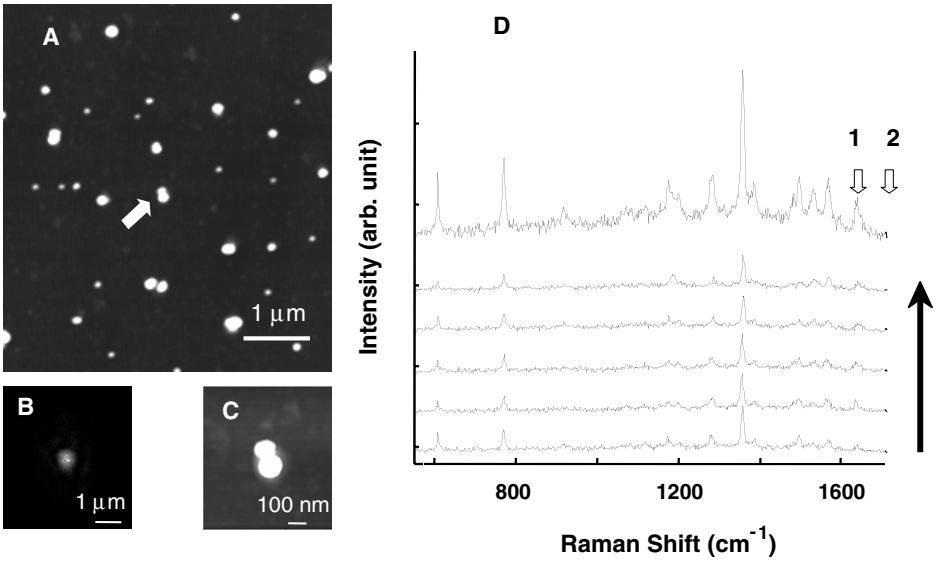

Figure 3. Correlated topographic and Raman spectroscopic imaging of Ag nanoparticles. (A) AFM image (5×5 μm^2, 256×256 pixels, 0.2 Hz scan rate) of Ag nanoparticles adsorbed with the rhodamine 6 G (R6G) molecules ($\sim$25 R6G per particle). (B) 2D Raman intensity image (5×5 μm^2, the same area as (A), 300×300 pixels, 1 ms per pixel) of the R6G molecules adsorbed on Ag nanoparticles at 514.5 nm linearly polarized excitation. The Raman signal was detected using an APD after a 25 nm bandwidth bandpass filter centred at 565 nm. It is evident that only the bi-particle cluster (marked by an arrow in (A) and zoomed in (C)) gives a strong Raman signal. Note that (B) is on the same imaging field of 5×5 μm^2, only scaled down in presentation. (C) Zoom-in AFM image (800×800 nm^2) of the bi-particle cluster indicated by an arrow in (A). Heights of the particles were measured as 60 nm (upper) and 80 nm (lower). (D) Five Raman spectra sequentially collected in 200 ms time increments from the same bi-particle cluster at 50 W cm^{-2} excitation. The top spectrum is the sum of the five spectra. The two arrows indicate the narrow-band spectral detection of (channel 1) Raman and background, and (channel 2) background. The Raman signal is to be picked up by taking the difference of the signals (channel 1 − channel 2). (Adapted with permission from the American Chemical Society from [60].)

(figure 3(C)); the other clusters either have gaps at the interstitial sites that are too large or have fused into one larger nanoparticle. Although the focus spot of the laser excitation is diffraction limited at 200–300 nm, the SERS spectra collected and the spectral fluctuation observed (figure 3(D)) are from a nanoscale interstitial site of a single Ag nanoparticle cluster [60, 62].

From correlated AFM and SERS microscopic imaging, the hot spots observed were identified as clusters of Ag nanoparticles under an average loading ratio of $\sim$1 to 50 R6G per Ag nanoparticle. By changing the loading concentration of the R6G from 10^{-10} to 10^{-6} M, we found that the Raman signal significantly dominated the fluorescence background when the coverage was a monolayer or less, whereas the fluorescence background dominated when the loading was more than a monolayer. Cytochrome c molecules gave a low fluorescence background and showed spectral fluctuations at hot spots under the up-to-25% coverage (10^{-9}–10^{-7} M) of the Ag nanoparticles. It is commonly observed that the multiple-molecule-loaded nanoparticles presented SERS fluctuation behaviour similar to that of previous reports for single-molecule SERS [50–52]. Specific Raman-band fluctuation could then be monitored by using two-channel photon-stamping recording with sub-microsecond time resolution [60, 62], switching the detection channel from spectrum collection using a charge-coupled device (CCD) camera to single-photon counting detection using avalanche photodetectors (APDs) (figure 1).

To further identify the origin of the Raman fluctuations at nanoscale sites, we measured Raman intensity trajectories at the 1650 cm^{-1} band of R6G at different laser excitation intensities for the single interstitial sites. The fluctuations were obvious in these single-site band-selective SERS intensity trajectories. About 10% of the trajectories also showed total Raman intensity blinking besides Raman intensity fluctuations that occurred more frequently when the excitation intensity was above 100 W cm^{-2} [60, 62]. We [60, 62] and other laboratories [51, 56] have observed that the Ag nanoclusters can give a white light continuum and luminescence under laser excitation, which gives a broad background for the Raman spectra that also blinks essentially in correlation with the Raman intensity blinking [51, 56, 60, 62]. This phenomenon has been reported previously, and it was suggested that tunnelling electronic interactions between the chemically adsorbed molecules and the metallic nanoparticle plasmon and the plasmon dephasing were responsible [21–26, 51, 56].

We concluded that the SERS spectral fluctuation is associated with the nanoscale confinement of the electromagnetic field enhancement that plays a major role in controlling a small number of molecules that may dominate the SERS signal and contribute to spectral fluctuation. The fluctuation amplitude significantly changes with the number of molecules confined at the nano-local hot field. We estimate the area of a two-sphere (80 nm diameter; Ag) interstitial junction to be about 50 nm^2, where more than 70% of the enhanced SERS signal originates. For example, only four to six cytochrome c molecules can be confined in an interstitial junction area that experiences a strong local electric field enhancement. Consequently, the intrinsic SERS fluctuation can be averaged out in an ensemble-averaged measurement when multiple hot spots contribute to the SERS signal.

4. SERS spectral fluctuation dynamics at interstitial sites of nanoparticle clusters

Fluctuation dynamics were found to be different from site to site [60, 62], where there are different interstitial shapes and spaces, particle sizes and shapes, polarizations, and cluster geometries. This is understandable in that the SERS enhancement is a local effect of the gradient and surface plasmon fields, defined by nanoparticle materials and their surface geometries, which are heterogeneous at the nanoscale [60, 62]. The Raman fluctuation rate was found to be highly inhomogeneous over individual interstitial sites associated with the heterogeneous geometry of the nanoclusters [60, 62]. To analyse the Raman fluctuation dynamics, we recorded Raman intensity time trajectories using two-channel APD single-photon detection at sub-microsecond time resolution, $\{I(t)\}$. Figure 4(A) shows a typical autocorrelation function, $C(t) = \langle \Delta I(0) \Delta I(t) \rangle / \langle \Delta I(0)^2 \rangle$, where $\Delta I(t) = I(t) - \langle I(t) \rangle$, deduced from a Raman intensity trajectory recorded from a single interstitial site of a Ag nanoparticle cluster. Its fluctuation rate constant was calculated to be 0.9 s^{-1} by fitting the autocorrelation with an exponential decay.

By changing the laser excitation intensity at individual hot interstitial sites of the nanoclusters, we observed that

(1) the SERS fluctuation dynamics are both photoinduced and spontaneous and
(2) the dependence of SERS fluctuation dynamics on the laser excitation intensity is different from site to site, although the photoinduced component dominated in a wide laser excitation intensity range above 50 W cm^{-2}.

This experiment was done by collecting R6G molecule Raman band (1650 cm^{-1}) intensity trajectories at different laser intensity excitations and then analysing the autocorrelation function decay rates. Plotting the autocorrelation function decay rate constant versus the laser excitation photon flux shows the dependence on the slope of the plot (figure 4(B)). The

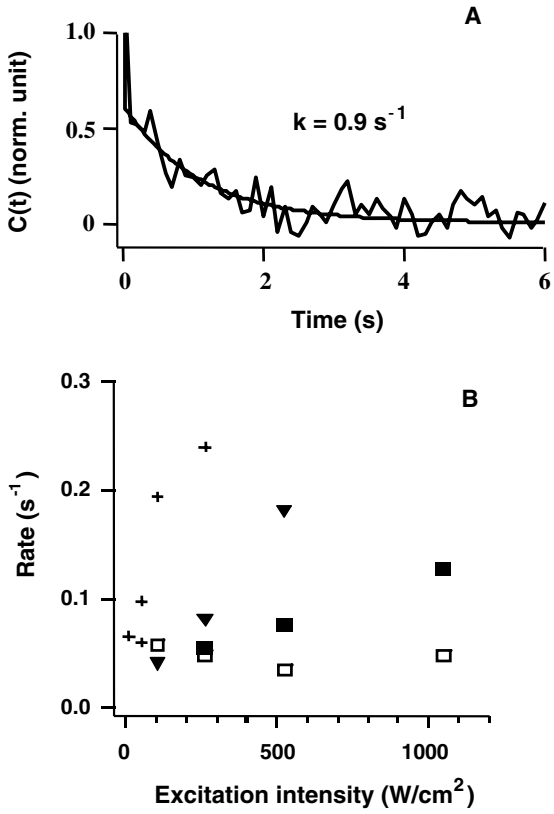

Figure 4. (A) The autocorrelation function calculated from a single nanocluster Raman intensity trajectory of R6G. (B) The excitation intensity dependence of the SERS fluctuation rate constant deduced from the R6G Raman intensity fluctuation trajectories of four individual Ag nanoclusters (∼25 R6G per particle; ∼0.2% coverage). It is evident that different nanoclusters have different dependences and different ratios of spontaneous and photoinduced fluctuations. (Adapted with permission from the American Chemical Society from [60].)

spontaneous rate constant, below $0.05 \pm 0.03\ s^{-1}$ for R6G (figure 4(B)), can be extrapolated from the intercept of the linear plot at a zero excitation photon flux [60, 62]. Typical plots deduced from four single nanoclusters are shown in figure 4(B). The laser excitation dependence varies from strongly dependent to insignificant from cluster to cluster, i.e., the SERS fluctuation dynamics are highly inhomogeneous. Presumably, the fluctuation rates were determined by the thermal motion rates of the Raman active molecules at the interstitial sites. The thermal motions, both photo-induced and spontaneous motions, should be sensitive to the interactions amongst the adsorbed molecules and the molecule–surface interactions at the interstitial sites. Apparently, the Raman fluctuations at some hot spots present dominated spontaneous behaviour (for example, figure 4(B), 'open' square) at the excitation intensity as high as $1000\ W\ cm^{-2}$. Currently, as the fundamental understanding of the SERS enhancement is still incomplete, we do not have a definitive experimental interpretation of the origins of the SERS fluctuation dynamics. The possible reasons for different sites having different fluctuation dynamics might be related to inhomogeneous interstitial site configurations, electromagnetic field distribution under laser illumination, or the thermal energy dissipation mechanism. Section 5 describes some of our computational simulations of these complex phenomena.

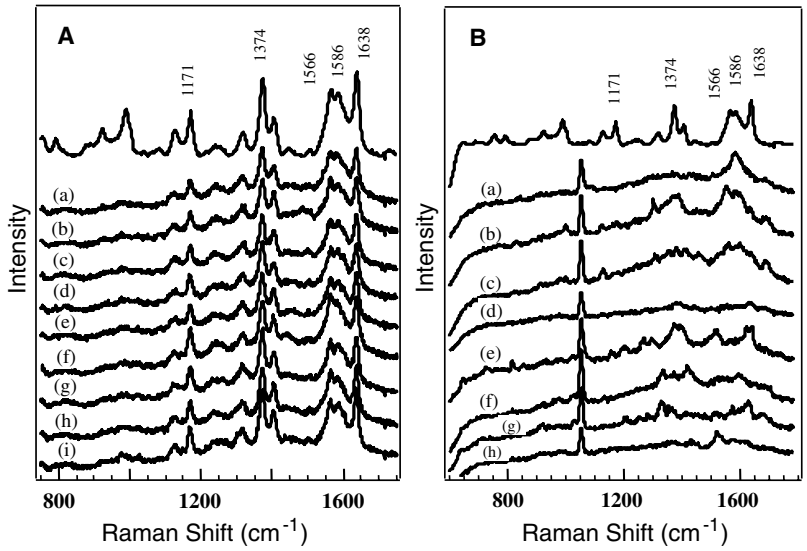

Figure 5. (A) Nine Raman spectra (a)–(i) sequentially collected in 1 s time increments from a single SERS-active Ag nanoparticle cluster sample incubated with 100 nM ferric cytochrome c at 50 W cm^{-2} excitation intensity. The top spectrum is a bulk SERS spectrum from a ferric cytochrome c sample. (B) Eight Raman spectra (a)–(h) sequentially collected in 1 s time increments from a single SERS-active Ag nanoparticle cluster sample incubated with 1 nM ferric cytochrome c at 380 W cm^{-2} excitation intensity. A sharp feature around 1050 cm^{-1} is from a glass impurity, which was used as an internal intensity standard. The top spectrum is a bulk SERS spectrum from a ferric cytochrome c sample for comparison. (Adapted with permission from the American Chemical Society from [60].)

The SERS fluctuation dynamics are predominantly photoinduced for cytochrome c at Ag nanoclusters, and the spontaneous fluctuation is not observable in our experiments [60, 62]. Figures 5(A) and (B) show the SERS spectra consecutively collected at 100 and 1 nM cytochrome c loading concentrations, respectively. An insignificant Raman spectral fluctuation at the 100 nM cytochrome c loading (figure 5(A)) becomes very significant at the 1 nM cytochrome c loading (figure 5(B)). The fluorescence background of cytochrome c is insignificant compared with the Raman signal [60, 62]. The SERS fluctuation rate of cytochrome c and the linear dependence of the fluctuation rate on the excitation intensity are also found to be inhomogeneous amongst the nanoclusters (figures 6(A)–(D)). However, there is no observable spontaneous fluctuation component (figures 6(C) and (D)) for cytochrome c SERS. The metalloporphyrin ring of cytochrome c is embedded in the protein matrix and not directly in contact with the Ag nanocluster surface. One of the possible reasons might be that the much larger size of the cytochrome c protein and its surface charge may result in the much higher activation barrier for significant spontaneous motions at ambient conditions.

The spontaneous and photoinduced Raman fluctuations are most likely associated with the spontaneous and photoinduced molecular motions at the interstitial sites. Discrete rotational and even translational motions can account for the Raman spectral fluctuations [50–52, 60, 62], especially for the fluctuation at the timescale of sub-seconds to seconds [51–53], as the Raman scattering intensity changes by many orders of magnitude as the molecular dipole changes orientation. The dipole motions perturbed the molecular–metal chemical interactions and the interactions of the molecules with the image dipole [21–26], the gradient field [60, 62, 77–81], and the surface plasmon [21–26, 52, 53]. There is a strong evanescent electromagnetic field

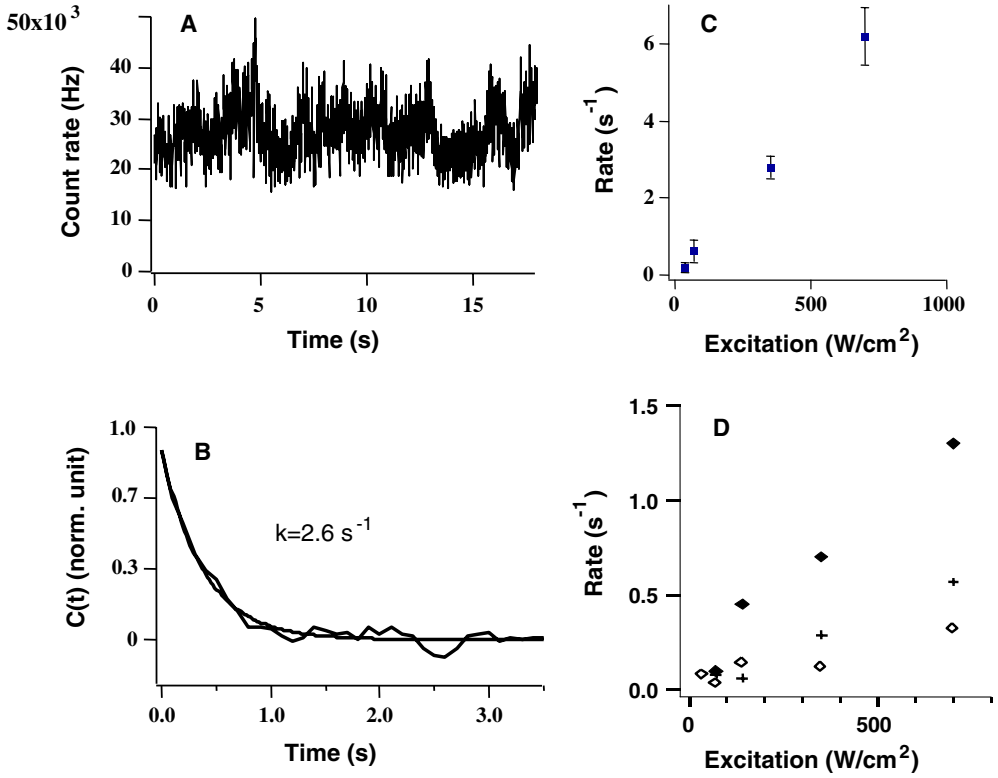

Figure 6. (A) A Raman total intensity trajectory of cytochrome c recorded from an interstitial site of a single Ag nanocluster. Raman intensity fluctuation is evident. (B) Autocorrelation function, $C(t)$, calculated from the Raman intensity trajectory in (A). (C) Excitation intensity dependence of the SERS fluctuation rate constant of cytochrome c for the same nanocluster in a higher excitation intensity and fluctuation rate regime. (D) The excitation intensity dependence of the SERS fluctuation rate constant deduced from the cytochrome c Raman total intensity fluctuation trajectories of three individual Ag nanoclusters (∼10% cytochrome c coverage of particles). It is evident that different nanoclusters have different dependences and there are no measurable spontaneous fluctuation components. (Adapted with permission from the American Chemical Society from [60].)

at the surface of the Ag nanoparticles, and the field gradient at the molecular scale can result in Raman scattering from the IR active vibration modes for molecules on the surface. The gradient-field SERS signal, which can be as large as the same amplitude of the normal SERS signal, is expected to contribute significantly to Raman scattering [60, 62, 77–81]. On the other hand, the ratio of the gradient-field Raman and normal Raman amplitudes can fluctuate as the molecules involve rotational motions. The ratio of the gradient Raman (G) and normal Raman (R) amplitudes is proportional to the field gradient $G/R = (\alpha/E)(\partial E/\partial q)$, where α is the molecular polarizability, E is the field, and $\partial E/\partial q$ is the gradient field. A vibrational mode will be Raman active when it has a polarizability component normal to the surface [60, 62, 77–81], which is apparently sensitive to the rotational motions of the adsorbed R6G molecules. The appearance and disappearance of the new Raman peaks (for example, figure 5(B)) that are not observable in an ensemble-averaged experiment have most likely originated from gradient-field Raman scattering.

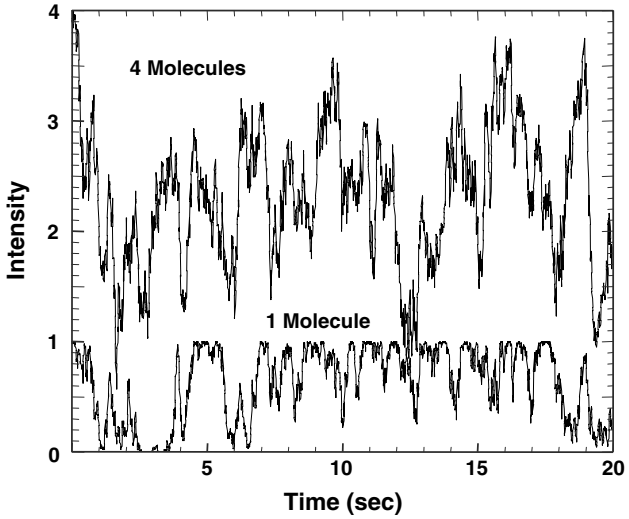

Figure 7. Simulated SERS intensity fluctuation when one molecule and four molecules are located in the interstitial site in figure 6(A). (Adapted with permission from the American Chemical Society from [60].)

To interpret the observed SERS fluctuation dynamics, we couple two types of calculations. The first, an optical multiple-scattering calculation, is used to estimate an observed intensity as a function of the configuration, which is defined in terms of molecular position and orientation, and the metallic sphere positions as a function of incident radiation wavelength and polarization (figures 2(A)–(C)). The second calculation is a rotational diffusion calculation used to construct an ensemble of time-correlated molecular configurations (figure 7). From these two calculations, simulated intensity trajectories as a function of time are constructed (figure 7). The fluctuations in this time series are then analysed using an autocorrelation function to determine the fluctuation dynamics.

To model the rotational diffusion, a random walk in orientation space was simulated using Monte Carlo sampling. Although our simulation considered only the electromagnetic field and its distribution effect on the SERS intensity fluctuation, the following rotational diffusion simulation should be applicable and relevant even when the chemical enhancement is also considered. The rotational probability distribution, $P(\theta, \phi; \tau)$, satisfies the rotational diffusion equation, $\partial_t P = D\nabla^2 P$, where ∇^2 is the angular part of the Laplacian operator in spherical coordinates. With

$$P(\theta, \phi; t = 0) = \frac{1}{2\pi}\delta(\cos\theta - 1),$$

it follows that the angular correlation functions give

$$\langle \cos\theta \rangle = \mathrm{e}^{-2Dt}, \qquad \text{and} \qquad \langle \cos^2\theta - \tfrac{1}{3} \rangle = \mathrm{e}^{-6Dt}.$$

The normalized correlation function, $\langle \delta I(t)\delta I(0)\rangle / \langle \delta I(0)\delta I(0)\rangle$ may be used to set the timescale for the rotational diffusion. Assuming that the rotational diffusion is the most significant source of fluctuations, we recover $D = 1\ \mathrm{s}^{-1}$ [60, 62].

The fluctuation amplitude significantly decreased with a number increase of molecules confined at the nano-local hot field, whereas the overall averaged signal increased. However, the fluctuation dynamics appeared the same, assuming that the fluctuations of individual molecules were independent [60, 62]. Assuming no interaction amongst the molecules, our

simulation indicates that the dynamics of $C_N(t)$, deduced from the multiple-molecule Raman fluctuation, are the same as those of $C(t)$ deduced from a single-molecule Raman fluctuation trajectory, except that the autocorrelation amplitude decreases linearly with the reverse number of molecules $(1/N)$, i.e., $C_N(t) = (1/N)C(t)$, where

$$C_N(t) = \langle \delta I_N(t) \delta I_N(0) \rangle / \langle I_N \rangle^2.$$

Applying this result to analyse the experimental SERS fluctuation trajectories, we are able to estimate the number of single molecules that contribute to the SERS fluctuation signal at an interstitial site. For example, observing that $\sqrt{\langle \delta I_N^2 \rangle}/\langle I_N \rangle \approx 0.33$ for the SERS fluctuation trajectory in figure 6(A), we estimate that $N = 4$ by comparing it to the simulated trajectories (figure 7). Our simulation suggests that SERS fluctuation can be observed at the coverage of multiple molecules per particle because a nanoscale interstitial site can only be occupied by a small number of molecules that may significantly contribute to the SERS and its fluctuation. For example, only four to six cytochrome c molecules can be confined in the interstitial junction area. Consequently, the SERS fluctuation can be averaged out in an ensemble-averaged measurement when multiple hot spots contribute to the SERS signal [60, 62]. Generally, as the number of contributing molecules increases, the overall signal level ($\langle I_N \rangle$) increases and the fluctuation amplitude standard deviation ($\sqrt{\langle \delta I_N^2 \rangle}$) and the relative amplitude ($\sqrt{\langle \delta I_N^2 \rangle}/\langle I_N \rangle$) decreased. Assuming that the interaction amongst the molecules is negligible, the overall signal level will linearly increase with the number of the contributing molecules, and the fluctuation amplitude standard deviation will eventually be buried in the measurement shot noise. Typically, in our measurements, we estimated that SERS fluctuations will be below the measurement noise if the number of contributing molecules is greater than about 10.

5. Local field enhancement at interstitial sites of nanoparticle clusters and nanostructures

In this section, we discuss our work on evaluating field distributions and enhancements at interstitial sites of metallic nanoparticles and nanostructures with different topographies, using a 'tip' under polarized laser excitation. The interstitial-site field distributions are highly sensitive to various parameters related to laser excitation fields and to nanostructure topographies and configurations. Such parameters are critical for a fundamental understanding of the Raman spectral fluctuations observed at the individual hot spots. To determine whether different clusters associated with inhomogeneous configurations yield inhomogeneous SERS fluctuation dynamics, it would be necessary to directly correlate nanoscale interstitial structures with SERS fluctuation dynamics. In the Mie-theory consideration discussed above, a metallic nanoparticle is assumed to be spherical or regular-shaped. Experimentally, however, it is still difficult to characterize electromagnetic field enhancement at nanoscale interstitial sites using SERS-correlated AFM imaging. The difficulties arise from the facts that (a) the interstitial site is typically embedded inside the nanoclusters and (b) the AFM spatial resolution cannot routinely resolve the molecular-scale surface configuration differences of the nanoclusters.

SERS Raman signals can be significantly enhanced by the antenna effect at near field, combined with surface plasmon enhancement. Thus, it is necessary to determine geometric configurations with respect to the incoming excitation beam in order to understand the geometric parameters of metallic nano-objects that provide high local electric field (E) enhancement. As the surface-enhanced Raman signal intensity is proportional to E^4, small variations in the electric field intensity induce dramatic changes in the Raman signal [21–26]. It is desirable, then, to simulate the electric field distribution by solving the system

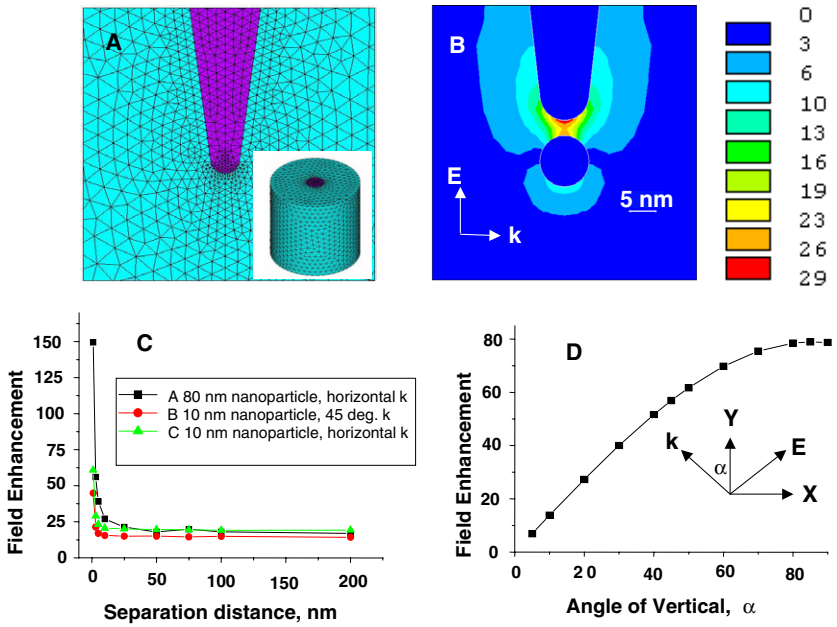

Figure 8. (A) Complete 3D mesh and the cross-section of the FEM model; Inset: electric field distribution around the AFM tip irradiated from the bottom (central cross-section of the 3D model). The mesh density was increased in the area of high curvatures and in the interfacial areas. In our simulation, the saturation condition of the mesh density was carefully evaluated and reached to ensure simulation accuracy. (B) Electric field distribution in the case of the tip positioned above the small nanoparticles (10 nm) illuminated sideways at a separation distance of 3 nm. Notations k and E represent the laser beam propagation vector and laser electric field vector, respectively. The material constant was based on the one used for Ag [82], $\varepsilon = -32.8 + 0.458\mathrm{i}$, with a laser beam wavelength of $\lambda = 810$ nm. The surrounding environment was modelled with $\varepsilon_0 = 1 + 1\mathrm{i}$ constant, to achieve the maximum transparency for the incoming laser beam and to avoid dumping field attenuation artifacts, which would result from signal attenuation before reaching the tip and/or nanoparticles. Field enhancement was in the vicinity of the Au AFM tip under the plane-wave laser illumination at 810 nm. (C) Graphical representation of dependence of the field enhancement of configuration on tip–particle distance. (D) Angular dependence of the electric field enhancement in the case of a Ag tip over single Ag nanoparticles. Diagram of E-field enhancement versus angle of laser beam propagation. (Adapted with permission from the American Chemical Society from [61].)

of Maxwell's equations for different geometric arrangements, dissecting the local field enhancement under various experimental configurations. There has been significant theoretical progress in numerically solving scattering problems of arbitrarily shaped nanoparticles, using such methods as the discrete dipole approximation [69], multiple multipoles [15], finite difference time domain [68, 72], time-domain finite elements [67], and frequency-domain finite elements [61, 63].

To estimate the volumes of electric field enhancements and their intensity distributions, we numerically characterized electromagnetic field enhancement at the typical clusters of metal nanoparticles, using the frequency-domain electromagnetic finite element method [61, 63]. Our model is based on a three-dimensional mesh, composed of tetrahedral (first-order) elements (figure 8(A)). The mesh density and size were optimized to the saturation point. The information sought from the simulation was the electric field enhancement defined as a ratio of the total to the incoming electric field intensities, $M = |E_{\mathrm{tot}}/E_0|$. Keeping the

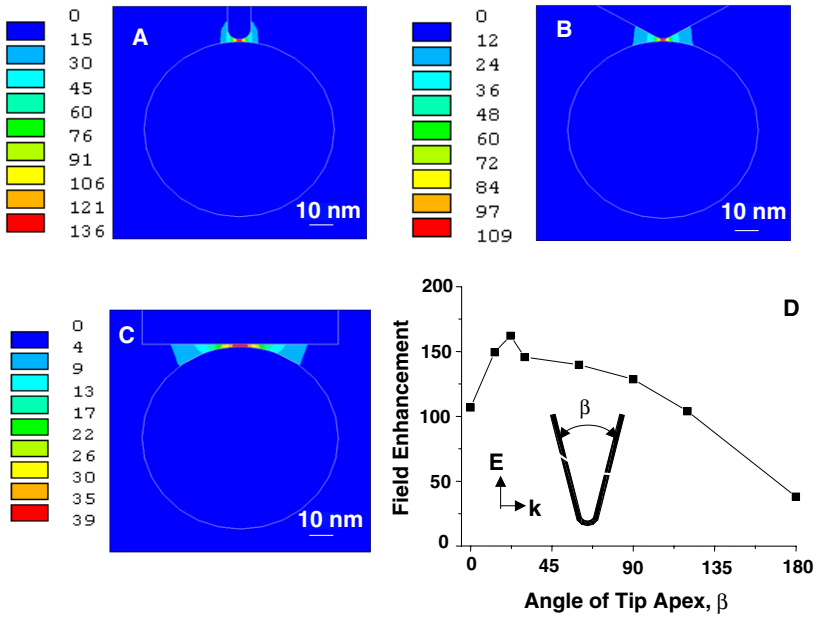

Figure 9. Influence of Ag tip apex angle change on the electric field enhancement (central cross-section of the 3D model). The tip is positioned on top of an 80 nm Ag nanoparticle. (A)–(C) Apex of 0° (in (A)), 120° (in (B)), and 180° (in (C)); (E) dependence of E-field enhancement versus tip apex angle (β). (Adapted with permission from the American Chemical Society from [61].)

intensity of the electric field of the incoming laser beam (E_0) to unity, we could consider the calculated electric field, E_{tot}, as numerically equivalent to the enhancement, M. We examined configurations consisting of a spherical particle and a tip nanostructure of various shapes at different interstitial distances and laser excitation angles.

Figure 8(B) represents an example simulation of various configurations, with the tip in the vicinity of the nanoparticles at a 5 nm particle–tip distance. With a change in the distance between the tip and the particle, the electric field enhancement changes (figure 8(C)). We found the field enhancement at interstitial sites to be similar for a wide range of particle sizes, from 10 to 80 nm, and the volume of maximal electric field enhancement to be within the same size range (figure 8(C)). The field enhancement is also sensitive to the electric field vector related to the interstitial site. We have simulated the same geometric configuration of the small particle and tip under a different excitation-laser propagation angle. Figure 8(D) shows the angular dependence of the intensity of electric field enhancement for a single particle (80 nm diameter) with the tip (5 nm apex radius) positioned above, at a distance of 2 nm. Enhancement saturation occurs when the propagation angle of the laser beam approaches the horizontal [61].

We have also examined field enhancements under different nanostructure topographies by evaluating their dependence on the tip apex divergence angle and found that the local field enhancement and distribution are not highly sensitive to tips of various sizes of apex. We modelled the influence of the tip size on the field enhancement, varying the tip apex angle from 0° to 180°, within a configuration consisting of the tip positioned 1 nm above a single nanoparticle (80 nm diameter). Figures 9(A)–(C) show the resulting distributions of the electric field for representative angles. Figure 9(D) shows the dependence curve of the field enhancement on the tip apex angle. Initially, with the increase of the tip apex angle, there is an increase in the intensity of the electric field enhancement. However, the total variation of

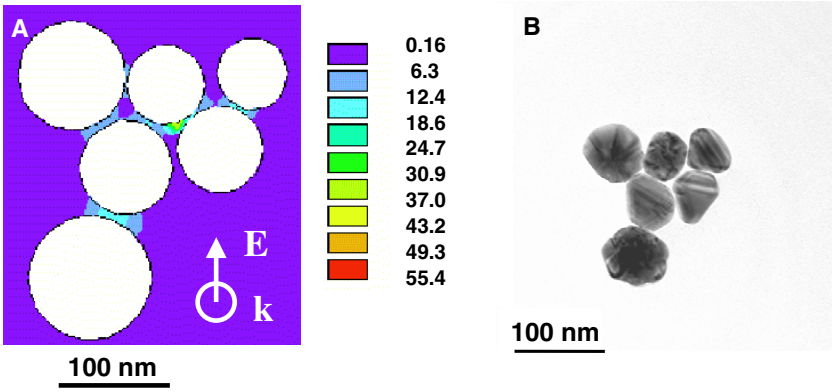

Figure 10. (A) Results of the FEM simulations of electric field enhancement distributions in the conjugated nanoparticle cluster. E and k represent the electric field vector and the propagation vector of the laser beam, respectively. (B) SEM images of a loosely conjugated Ag nanoparticulate cluster. (Adapted with permission from the American Chemical Society from [62].)

the electric field enhancement remains relatively small, about 30% within the range of applied angles from 0° to 120°. Thus, there is no significant gain in field enhancement when the tip shape is varied amongst ultra-sharp, whisker, or nano-tube tips.

FEM simulation is powerful in calculating the field distribution of complex configurations of nanoparticles and nanostructures, such as clusters. Figure 10(A) shows the results of the electric field distribution of a system comprising a cluster of nanoparticles of various sizes and overall configurations, according to the scanning electronic microscopy image in figure 10(B). As it was modelled, the propagation and polarization vectors were kept within the X–Y plane. Because it was assumed that the centre of all the particles was situated on the X–Y plane, the Z offset effects are ignored. The interesting feature of the results is that there are many orientations of the interstitial field polarizations for high enhancement, depending on how the laser polarization vector aligns with the minimum particle separation distance vectors. It is also apparent from the simulation that the enhancement factor is different among individual interstitial sites and that the distribution of the field enhancement would change as the laser polarization vector changes orientation.

This simulation provides two useful insights: (a) the existence of multiple hot spots within a single nanocluster is possible and (b) the hot spot distribution may also change as the laser polarization changes. The latter point is especially important in the case of a cluster of nanoparticles under SERS excitation because a small change in polarization and propagation vector of the laser excitation will induce a large shift in the position of the site of high enhancement. This deserves careful consideration when a result dependent on laser polarization is analysed since a different interstitial site could be sampled for the same nanoparticle cluster as the excitation polarization is being changed. It is logical to expect that in a certain configuration only one spot at a time within the radius of the excitation laser beam will provide enough electric field enhancements to produce a distinguishable Raman signal.

In typical SERS measurements under more heterogeneous systems, rough metallic surfaces are often used to enhance the Raman signals. SERS spectral fluctuations can be observed at the optical-diffraction-limited imaging spots. To provide insight into which kind of fractal surface provides high near-field enhancement and to explore the detailed distributions in near-field enhancement with various generations of fractal iterations representing the roughness of surfaces, we simulated the influence of different surface morphologies on electromagnetic

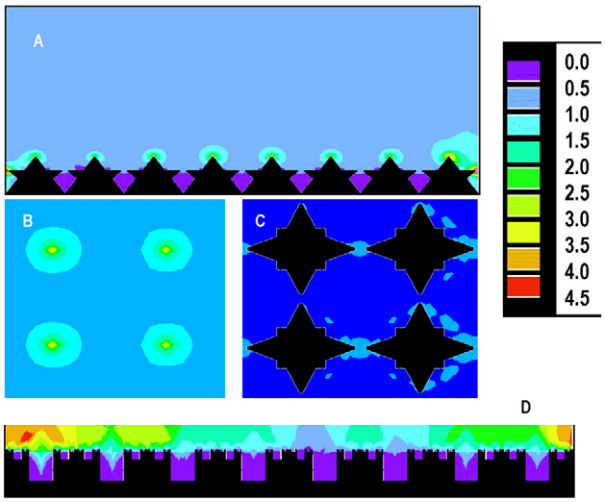

Figure 11. Near-field enhancement distributions of the second-order generation simulations of a dentritic surface, Au in vacuum, irradiated with an 810 nm plane wave at 45° propagation of the surface normal vector: (A) side-view cross-section of the three-dimensional model; (B) top-view cross-section of the three-dimensional model, at the level of the top apex; and (C) top-view cross-section at the level of smaller dendritic apexes. The mesh of the models presented here extended to 400 nm above the surface, or half the wavelength, in order to minimize boundary influences. The pyramidal fractal base for the dendritic fractals was 80 nm (height and base). The basic motif of the sponge model had a characteristic size of $270 \times 90 \times 30$ nm^3. Both types were arrayed in 8×8 patterns. The laser beam was represented as a plane wave. We used experimentally determined frequency-dependent material dielectric constants, obtained from an experimental measurement of noble metal thin film optical properties [82]. (D) Near-field enhancement distributions of the third-order generation simulations of adsorber surface: cross-section through the centre of the finite element Menger-mesh model. (Adapted with permission from the American Chemical Society from [63].)

field enhancements at the rough surfaces of noble metals and also evaluated the optimal conditions for the generation of a surface-enhanced Raman signal of absorbed species on a metallic substrate [63]. Two different classes of surfaces were analysed using fractal models and finite electromagnetic element method simulation, representing dendritic and sponge-like structures [63]. Our simulations (figure 11) showed that while the dendritic fractals enhanced the near-field electromagnetic field the sponge fractals significantly reduced the local electromagnetic field intensity. Moreover, the orders of the fractal objects did not significantly alter the total enhancement, and the distribution of a near-field enhancement was essentially invariant to the changes in the angle of an incoming laser beam [63].

Figures 11(A)–(C) show FEM simulation results of the electric field enhancement distributions of the second-order fractal under 45° incident laser illumination. The second-order fractal model consisted of the topographic grid of the regular square-based pyramids with down-scaled pyramids positioned on it [63]. The lightning-rod effect is clearly observable, with the approximately threefold enhancement concentrated at the tips of the pyramids (figures 11(A)–(C)). The distribution volume of the local field enhancement is constrained within about 10 nm from the surface around the tips of the pyramids. In contrast, the electromagnetic field is significantly depleted at the bottom of the pyramids, as well as in the interstitial spaces (figures 11(A) and (C)). The field depletion in the interstitial space differed significantly from the interstitial-site field enhancement of the isolated nanoparticle

clusters under laser illumination. By varying the incoming laser beam incident angle, from 0° to 90°, we observed no significant change in the absolute intensity and distribution shape of the near-field enhancement in the surface vicinity. Thus, on the densely populated surface with dendrites of fractal geometry, the near-field enhancement is insensitive to the direction of incoming laser beam propagation vectors.

In the sponge fractal, instead of electric near-field enhancement, we observed strong near-field depletion, in the range of one order of magnitude in close proximity to the metal surface. The electric field attenuation is strongest within the pore, which could be explained partially in terms of the 'Faraday cage' effect. The same behaviour is observed over the range of laser excitation wavelengths, which indicates that the sponge acts as a very broadband attenuator.

There is nevertheless a large inhomogeneity in the near-field distribution in the nanoscale vicinity of the rough metallic surfaces. This is especially important in considering the results of the SERS experiments of highly diluted samples as well as of single molecules. Most of the area at the bottom of surfaces is actually field depleted, where the molecules will not only have no surface enhancement but also have depleted excitation. It is most likely that the SERS signal detected from the far field is dominated by the molecules located on the tops of the dendritic apexes on the surface, with little or no contribution from the molecules in the grooves or cavities of the rough surface. Only the molecules that are absorbed close to the high apexes of dendritic aggregates will be exposed to an electric field of sufficient strength to make them SERS active [50–52, 59, 60, 62]. As the molecules are capable of diffusing on the metallic surface, they will be constantly going in and out of the volume of the high electric near-field enhancement, which may significantly contribute to the experimentally observed Raman fluctuations when only a single hot spot is examined under microscopic measurements. This conclusion holds not only for single-molecule SERS but also generally for multiple molecules with thermal motions within a non-uniform evanescent field in nanoscale topographic inhomogeneities.

6. Summary and perspectives

SERS fluctuation dynamics have proven to be highly inhomogeneous amongst individual nanoparticle clusters due to the inhomogeneous chemical interactions of the substrates and molecules, heterogeneous surface geometry and interstitial site structures, nanoscale confinement of the molecules at the interstitial sites, and complex laser electromagnetic field interactions with the clusters. Fluctuation dynamics differ from site to site, where there are different interstitial shapes and spaces, particle sizes and shapes, cluster geometries, and transition dipoles. The SERS spectral fluctuation is typically both photoinduced and spontaneous. Although the fluctuation above $\sim$50 W cm^{-2} excitation is often dominated by photoinduced processes, spontaneous fluctuation associated with molecular conformational change dynamics can be measured at lower excitation intensity. The ratio of spontaneous and photoinduced fluctuation was also site dependent, presumably dependent on the local field enhancement and the heterogeneous nanoscale geometry varying from cluster to cluster. The origins of the SERS fluctuations could be due to the photoinduced and spontaneous discrete rotational and translational motions of the molecules and their interactions with the local electromagnetic field and substrate surfaces, which in turn depend on the complexity of the nanoscale interstitial structures. Spectral fluctuations can be observable from Ag or Au nanoparticles in a wide range, from one molecule to hundreds of molecules, or even sub-monolayer, per particle. For example, we observed that the SERS fluctuation behaviour can exist for Ag nanoparticles up to 25% of monolayer coverage of cytochrome c. It is the nanoscale confinement of the local electromagnetic field and chemical interactions that define

the SERS fluctuations, and the nanoscale confined interstitial sites control a small number of the molecules that can give a SERS-dominated signal and fluctuations. Single-molecule fluorescence fluctuations are powerful in revealing molecular conformational dynamics [36–45], and Raman fluctuation spectroscopy can be expected to be even more informative and unique in measuring molecular conformational changes and dynamics. Our simulation and model analysis suggest that the SERS fluctuations show more occurrences of blinking at the single-molecule level versus the multiple-molecule level and that the fluctuation amplitude decreases as the number of signal-contributing molecules increases. This method is more versatile than probing Raman fluctuation dynamics because the nanoscale confinement at interstitial sites controls a low number of molecules that predominately contribute to the Raman signal detected from the far field. In other words, a Raman spectrum from a single Raman-active molecule typically shows significant fluctuation, but an observation of Raman spectral fluctuation is not sufficient to exclusively identify the single-molecule origin of a Raman spectrum. Nevertheless, an autocorrelation function analysis of Raman fluctuation dynamics can yield the same information on fluctuation dynamics from multiple molecules as can be obtained from a single molecule, as long as the molecule motions are independent and homogeneous.

Site-specific Raman spectroscopy and imaging have significantly advanced in recent years. There are now two major frontiers, technology development and scientific applications. Technical development has made tremendous progress in the areas of imaging sensitivity, selectivity, time resolution, and spatial resolution. For example, high spatially resolved correlated Raman and topographic imaging have been demonstrated for single-walled carbon nanotubes [13], and the metallic tip enhancement on the Raman signal has been improved dramatically, up to about 10^6 times on imaging CN^- and MGITC dye molecules at Au surfaces under electronic current tunnelling through a Au tip [83]. It has been demonstrated routinely at laboratories worldwide that NSOM Raman imaging can reach a spatial resolution of approximately 20–50 nm. This imaging technique will continue to advance in years to come.

There are also significant developments in applications of site-specific Raman spectroscopy because of extensive research in material science, surface chemistry, catalysis, and biological system analyses, among other areas. Future significant scientific applications will primarily be in the area of dissecting the inhomogeneous chemical and biological systems under heterogeneous environments:

(1) nanoscale characterization of the protein distributions and identification of protein species and their reactivities on the outer membranes of living cells [19, 84];
(2) site-specific catalysis on reaction dynamics with detailed topographic mapping, adsorption state identification, and Franck–Condon coupling specifications [35]; and
(3) interfacial redox electron transfer reactions by probing specific redox states of the reactants at interfaces at specific local sites of chemical and biological systems [85].

Applications of tip-enhanced Raman imaging and site-specific Raman spectroscopy for the study of chemistry, biophysics, and biology at interfaces and on surfaces will no doubt undergo significant advancements.

Acknowledgments

The author thanks Miodrag Micic, Nicholas Klymyshyn, Greg Schenter, Yung Doug Suh, Leyung Zhu, and Dehong Hu for their crucial contributions to the work discussed here. This work was supported by the Chemical Sciences Division of the Office of Basic Energy Sciences within the Office of Science of the US Department of Energy (DOE), and supported by

the Laboratory Directed Research and Development Program of Pacific Northwest National Laboratory. The Pacific Northwest National Laboratory is operated by Battelle Memorial Institute for DOE under contract DE-AC06-76RLO1830.

References

[1] For a review, Birdi K S 2003 *Scanning Probe Microscopes–Applications in Science and Technology* (London: CRC Press)
[2] Courjon D 2003 *Near Field Microscopy and Near Field Optics* 1st edn (London: Imperial College Press)
[3] Ohtsu M 1998 *Near-Field Nano/Atom Optics and Technology* 1st edn (New York: Springer)
[4] Paesler M A and Moyer P J 1996 *Near-Field Optics: Theory, Instrumentation and Applications* (New York: Wiley)
[5] Dunn R C 1999 Near-field scanning optical microscopy *Chem. Rev.* **99** 2891
[6] Inouye Y 2001 Apertureless metallic probes for near-field microscopy *Top. Appl. Phys.* **81** 29–48
[7] Kawata S 2001 Near-field microscope probes utilizing surface plasmon polaritons *Top. Appl. Phys.* **81** 15–27
[8] Hayazawa N, Inouye Y, Sekkat Z and Kawata S 2001 Near-field Raman scattering enhanced by a metallized tip *Chem. Phys. Lett.* **305** 369–74
[9] Collier C P, Saykally R J, Shiang J J, Henrichs S E and Heath J R 1997 Reversible tuning of silver quantum dot monolayers through the metal–insulator transition *Science* **277** 1978
[10] Anderson M S 2000 Locally enhanced Raman spectroscopy with an atomic force microscope *Appl. Phys. Lett.* **76** 3130–2
[11] Stöckle R M, Suh Y D, Deckert V and Zenobi R 2000 Nanoscale chemical analysis by tip-enhanced Raman spectroscopy *Chem. Phys. Lett.* **318** 131–6
[12] Anderson M S and Pike W T 2002 A Raman-atomic force microscope for apertureless-near-field spectroscopy and optical trapping *Rev. Sci. Instrum.* **73** 1198–203
[13] Hartschuh A, Sanchez E J, Xie X S and Novotny L 2003 High-resolution near-field Raman microscopy of single-walled carbon nanotubes *Phys. Rev. Lett.* **90** 095503
[14] Richards D, Milner R G, Huang F and Festy F 2003 Tip-enhanced Raman microscopy: practicalities and limitations *J. Raman Spectrosc.* **34** 663–7
[15] Novotny L, Bian R and Xie X S 1997 Theory of nanometric optical tweezers *Phys. Rev. Lett.* **79** 645–8
[16] Pettinger B, Picardi G, Schuster R and Ertl G 2002 Surface-enhanced and STM-tip-enhanced Raman spectroscopy at metal surfaces *Single Mol.* **3** 285
[17] Hu D, Micic M, Klymyshyn N, Suh Y D and Lu H P 2003 Correlated topographic and spectroscopic imaging beyond diffraction limit by atomic force microscopy metallic tip-enhanced near-field fluorescence lifetime microscopy *Rev. Sci. Instrum.* **74** 3347–55
[18] Trabesinger W, Kramer A, Kreiter M, Hecht B and Wild U P 2002 Single-molecule near-field optical energy transfer microscopy *Appl. Phys. Lett.* **81** 2118–20
[19] Micic M, Hu D, Newton G, Romine M and Lu H P 2004 Correlated atomic force microscopy and fluorescence lifetime imaging of live bacterial cells *Surf. Colloids.* B **34** 205–12
[20] Hu D, Micic M, Klymyshyn N, Suh Y D and Lu H P 2004 Correlated topographic and spectroscopic imaging by combined atomic force microscopy and optical microscopy *J. Lumin.* **107** 4–12
[21] Gersten J and Nitzan A 1980 Electromagnetic theory of enhanced Raman scattering by molecules adsorbed on rough surfaces *J. Chem. Phys.* **73** 3023–37
[22] Kneipp K, Kneipp H, Itzkan I, Dasari R R and Feld M S 1999 Ultrasensitive chemical analysis by Raman spectroscopy *Chem. Rev.* **99** 2957–76
[23] Campion A and Kambhampati P 1998 Surface-enhanced Raman scattering *Chem. Soc. Rev.* **27** 241–50
[24] Jiang J, Bosnick K, Maillard M and Brus L 2003 Single molecule Raman spectroscopy at the junctions of large Ag nanocrystals *J. Phys. Chem.* B **107** 9964–72
[25] Muniz-Miranda M 2002 SERS effect from silver photoreduced on to silica colloidal nanoparticles *J. Raman Spectrosc.* **33** 295–7
[26] Otto A 2002 What is observed in single molecule SERS, and why? *J. Raman Spectrosc.* **33** 593–8
[27] For a review, Hupp J T and Williams R D 2001 Using resonance Raman spectroscopy to examine vibrational barriers to electron transfer and electronic delocalization *Acc. Chem. Res.* **34** 808–17
[28] Wootton J L and Zink J I 1997 Unusual intensities in the resonance Raman spectra and excitation profiles of an intervalence metal-to-metal charge transfer complex *J. Am. Chem. Soc.* **119** 1895–900
[29] Mrozek M F, Wasileski S A and Weaver M J 2001 Periodic trends in electrode–chemisorbate bonding: Benzonitrile on platinum-group and other noble metals as probed by surface-enhanced Raman spectroscopy combined with density functional theory *J. Am. Chem. Soc.* **123** 12817–25

[30] Heller E J 1981 The semiclassical way to molecule spectroscopy *Acc. Chem. Res.* **14** 368–874
[31] Myers A B 1997 Resonance Raman intensity analysis of excited-state dynamics *Acc. Chem. Res.* **30** 519–25
[32] Schatz G C 1984 Theoretical studies of surface enhanced Raman scattering *Acc. Chem. Res.* **17** 370–6
[33] Kim W, Safonov V P, Shalaev V M and Armstrong R L 1999 Fractals in microcavities: giant coupled, multiplicative enhancement of optical responses *Phys. Rev. Lett.* **82** 4811–4
[34] Lu H, Petrov V and Hupp J T 1995 Intervalence excitation of the Creutz–Taube ion. Resonance Raman and time-dependent scattering studies of Franck–Condon effects *Chem. Phys. Lett.* **235** 521–7
[35] Pan D, Hu D and Lu H P 2005 Probing inhomogeneous vibrational relaxation energy barriers of interfacial electron transfer, submitted
[36] Lu H P, Xun L and Xie X S 1998 Single-molecule enzymatic dynamics *Science* **282** 1877
[37] Lu H P and Xie X S 1997 Single-molecule kinetics of interfacial electron transfer *J. Phys. Chem.* A **101** 2753
[38] Lu H P and Xie X S 1997 Single-molecule spectral fluctuations at room temperature *Nature* **385** 143–6
[39] Lu H P, Iakoucheva L M and Ackerman E J 2001 Single-molecule conformational dynamics of fluctuating noncovalent DNA–protein interactions in DNA damage recognition *J. Am. Chem. Soc.* **123** 9184–5
[40] Hu D and Lu H P 2003 Single-molecule nanosecond anisotropy dynamics of tethered protein motions *J. Phys. Chem.* B **107** 618–26
[41] Harms G S, Orr G, Montal M, Thrall B D, Colson S D and Lu H P 2003 Probing conformational changes of gramicidin ion channels by single-molecule patch-clamp fluorescence microscopy *Biophys. J.* **85** 1826
[42] Tan X, Nalbant P, Toutchkine A, Hu D, Vorpagel E R, Hahn K M and Lu H P 2004 Single-molecule study of protein–protein interaction dynamics in a cell signaling system *J. Phys. Chem.* B **108** 737–44
[43] Xie X S and Trautman J K 1998 Optical studies of single molecules at room temperature *Annu. Rev. Phys. Chem.* **49** 441–80
[44] Moerner W E and Orrit M 1999 Illuminating single molecules in condensed matter *Science* **283** 1670–6
[45] Rigler R, Orrit M and Basche T 2003 *Single Molecule Spectroscopy: Nobel Conference Lectures* (Berlin: Springer)
[46] For a review, Turrell G and Corset J 1996 *Raman Microscopy: Developments and Applications* (New York: Academic)
[47] For a review, Pelletier M J 1999 *Analytical Applications of Raman Spectroscopy* (Oxford: Blackwell Science)
[48] For a review, Clark J H and Hester R E 1993 *Biomolecular Spectroscopy* (New York: Wiley)
[49] Kneipp K *et al* 1996 Population pumping of excited vibrational states by spontaneous surface-enhanced Raman scattering *Phys. Rev. Lett.* **76** 2444–7
[50] Nie S and Emory S R 1997 Probing single molecules and single nanoparticles by surface-enhanced Raman scattering *Science* **275** 1102–6
[51] Michaels A M, Nirmal M and Brus L E 1999 Surface enhanced Raman spectroscopy of individual rhodamine 6G molecules on large Ag nanocrystals *J. Am. Chem. Soc.* **121** 9932–9
[52] Xu H, Bjerneld E J, Käll M and Borjesson L 1999 Spectroscopy of single hemoglobin molecules by surface enhanced Raman scattering *Phys. Rev. Lett.* **83** 4357–60
[53] Xu H, Aizpurua J, Käll M and Apell P 2000 *Phys. Rev.* E **62** 4318–24
[54] Bjerneld E J, Foldes-Papp Z, Kall M and Rigler R 2002 Single-molecule surface-enhanced Raman and fluorescence correlation spectroscopy of horseradish peroxidase *J. Phys. Chem.* B **106** 1213–8
[55] Moyer P J, Schmidt J, Eng L M, Meixner A J, Sandmann G W, Dietz H and Plieth W 2000 Surface-enhanced Raman scattering spectroscopy of single carbon domains on individual Ag nanoparticles on a 25 ms time scale *J. Am. Chem. Soc.* **122** 5409–10
[56] Michaels A M, Jiang J and Brus L 2000 Ag nanocrystal junctions as the site for surface-enhanced Raman scattering of single rhodamine 6G molecules *J. Phys. Chem.* B **104** 11965–71
[57] Eggeling C, Schaffer J, Seidel C A M, Korte J, Brehm G, Scheider S and Schrof W 2001 Homogeneity, transport, and signal properties of single Ag particles studied by single-molecule surface-enhanced resonance Raman scattering *J. Phys. Chem.* A **105** 3673–9
[58] Xu H and Kall M 2002 Surface-plasmon-enhanced optical forces in silver nanoaggregates *Phys. Rev. Lett.* **89** 246802
[59] Weiss A and Haran G 2001 Time-dependent single-molecule Raman scattering as a probe of surface dynamics *J. Phys. Chem.* B **105** 12348–54
[60] Suh Y D, Schenter G K, Zhu L and Lu H P 2003 Probing nano-surface enhanced Raman scattering fluctuation dynamics using correlated AFM and confocal ultramicroscopy *Ultramicroscopy* **97** 89–102
[61] Micic M, Klymyshyn N, Suh Y D and Lu H P 2003 Finite element method simulation of the field distribution for AFM tip-enhanced surface enhanced Raman scanning microscopy *J. Phys. Chem.* B **107** 1574
[62] Zhu L, Schenter G K, Micic M, Suh Y D, Klymyshyn N and Lu H P 2003 Nano-surface enhanced Raman scattering fluctuation dynamics *Proc. SPIE* **4962** 70–7

[63] Micic M, Klymyshyn N and Lu H P 2004 Finite element method simulations of the near-field enhancement at the vicinity of fractal rough metallic surfaces *J. Phys. Chem.* B **108** 2939–47
[64] Van Duyne R P, Hulteen J C and Treichel D A 1993 *J. Chem. Phys.* **99** 2101
[65] Malinsky M D, Kelly K L, Schatz G C and Van Duyne R P 2001 Nanosphere lithography: effect of substrate on the localized surface plasmon resonance spectrum of silver nanoparticles *J. Phys. Chem.* B **105** 2343–50
[66] Malinsky M D, Kelly K L, Schatz G C and Van Duyne R P 2001 Chain length dependence and sensing capabilities of the localized surface plasmon resonance of silver nanoparticles chemically modified with alkanethiol self-assembled monolayers *J. Am. Chem. Soc.* **123** 1471–82
[67] Martin Y C, Hamman H F and Wickramasinghe H K 2001 Strength of the electric field in apertureless near-field optical microscopy *J. Appl. Phys.* **89** 5774–8
[68] Krug J T, Sanchez E J, Xie X S and Leung P T 2002 Design of near-field optical probes with optimal field enhancement by finite difference time domain electromagnetic simulation *J. Chem. Phys.* **116** 10895–901
[69] Kelly L K, Coronado E, Zhao L L and Schatz G C 2003 The optical properties of metal nanoparticles: the influence of size, shape, and dielectric environment *J. Phys. Chem.* B **107** 668–77
[70] Hallen H D and Jahncke C L 2003 The electric field at the apex of a near-field probe: implications for nano-Raman spectroscopy *J. Raman Spectrosc.* **34** 655–62
[71] Milner R G and Richard D 2001 *J. Microsc.* **202** 66
[72] Bian R X, Dunn R C, Xie X S and Leung P T 1995 Single molecule emission characteristics in near-field microscopy *Phys. Rev. Lett.* **75** 4772–5
[73] Xu H, Azipurua J, Kall M and Appel P 2000 Electromagnetic contributions to single-molecule sensitivity in surface-enhanced Raman scattering *Phys. Rev.* E **62** 4318–24
[74] Stratton J A 1941 *Electromagnetic Theory* (New York: McGraw-Hill)
[75] Ohtaka K and Inoue M 1982 Electromagnetic aspects of the enhanced Raman scattering by a molecule adsorbed on a polarizable sphere *J. Phys. C: Solid State Phys.* **15** 6463–80
[76] Bohren C F and Huffman D R 1983 *Absorption and Scattering of Light by Small Particles* (New York: Wiley–Interscience)
[77] Ayars E J, Jahncke C L, Paesler M A and Hallen H D 2000 *J. Microsc.* **202** 142
[78] Ayars E J, Hallen H D and Jahncke C L 2000 Electric field gradient effects in Raman spectroscopy *Phys. Rev. Lett.* **85** 4180–3
[79] Wessel J 1985 Surface-enhanced optical microscopy *J. Opt. Soc. Am.* B **2** 1538–41
[80] Sharp S L, Warnack R J, Goudonnet J P, Lee I and Ferrell T L 1993 Spectroscopy and imaging using the photon scanning-tunneling microscope *Acc. Chem. Res.* **26** 377–82
[81] Jahncke C L, Paesler M A and Hallen H D 1995 Raman imaging with near-field scanning optical microscopy *Appl. Phys. Lett.* **67** 2483–5
[82] Johnson P B and Christy R W 1972 Optical constants of the noble metals *Phys. Rev.* B **6** 4370–9
[83] Pettinger B, Ren B, Picardi G, Schuster R and Ertl G 2004 Nanoscale probing of adsorbed species by tip-enhanced Raman spectroscopy *Phys. Rev. Lett.* **92** 096101
[84] Gorby Y, Biju V, Pan D, Fredrickson J, Mclean J J, Saffarini D and Lu H P 2005 Display and retraction of 'Outer Membrane' cytochromes by *Shewanella oneidensis* in response to electron acceptor availability, submitted
[85] Pan D, Klymyshyn N, Hu D and Lu H P 2005 Correlated AFM and Raman analyses of Franck–Condon barriers of interfacial electron transfer, submitted